mater.scichina.com link.springer.com

Published online 14 February 2022 | https://doi.org/10.1007/s40843-021-1931-0
Sci China Mater 2022, 65(6): 1443–1452

Hierarchical $Sb_2S_3/SnS_2/C$ heterostructure with improved performance for sodium-ion batteries

Rui Jia[1,2], La Li[2], Guozhen Shen[2*] and Di Chen[1*]

ABSTRACT Metal sulfides are promising anode materials for sodium-ion batteries (SIBs) because of their high theoretical capacities. However, they are usually limited by their poor cycling performance and rate properties due to their large volume expansion and sluggish reaction kinetics. Herein, $Sb_2S_3/SnS_2/C$ heterostructures were fabricated by directly growing SnS_2 nanoplates on Sb_2S_3 nanorods and then coating their surface with a carbon layer. Sodium-ion diffusion in several electrodes and different electrolytes was further evaluated to investigate the electrochemical performance of the heterostructures. Results revealed that the heterostructures greatly enhanced material stability and promoted ion and electron transport. Consequently, the $Sb_2S_3/SnS_2/C$ composites displayed a high reversible capacity of 642 mA h g^{-1} at a current density of 1 A g^{-1} after 600 cycles and a good rate performance of 367.3 mA h g^{-1} at 4 A g^{-1} in a $NaPF_6$-diglyme electrolyte. Therefore, $Sb_2S_3/SnS_2/C$ heterostructures are promising anode materials for SIBs.

Keywords: $Sb_2S_3/SnS_2/C$ heterostructures, anode, electrolyte, sodium-ion battery

INTRODUCTION

Energy storage plays an increasingly important role in our daily life. At present, the main power units of portable electronics, electric vehicles, and home appliances are lithium-ion batteries, whose development is restricted by their high price and limited resources [1–6]. As a substitute, sodium-ion batteries (SIBs) can be used for energy storage and have attracted wide attention. However, SIBs still face the problem of unsatisfactory electrochemical performance because of the large radius of sodium ion [7–9]. Thus, more suitable electrode materials and systems should be developed for high-performance energy storage devices.

Previous studies extensively investigated various electrode materials, including carbon materials, metal oxides, alloys, and metal sulfides [10–15]. Among them, metal sulfides have been profoundly explored because of their high theoretical capacity, low cost, and variety. For instance, Sb_2S_3 and SnS_2 have high theoretical capacities of 946 and 1136 mA h g^{-1}, respectively, and they participate in conversion and alloying reactions [16,17]. However, the sluggish reaction kinetics of Na^+ in bulk SnS_2 and Sb_2S_3 limit the rate of sodiation/desodiation, resulting in a low power density. Additionally, the large volume expansion during sodium-ion insertion/extraction can cause serious damage to electrodes and yield a poor electrochemical cycling performance. As such, efforts have been devoted to improving the electrochemical properties of devices by preparing special micro/nanostructures and introducing carbon materials [18–23]. Furthermore, constructing metallic sulfide-based heterostructures can effectively relieve internal pressure and maintain structural integrity during ion intercalation/de-intercalation. Introducing carbon layers helps enhance the electrical conductivity and buffer volume expansion of electrode materials. For example, Xu and co-workers [22] synthesized a Sb_2S_3/MoS_2 heterostructure as an anode material for SIBs. They obtained an initial reversible capacity of 701 mA h g^{-1} at a current density of 100 mA g^{-1}. Yin's group [23] fabricated a ZnS-Sb_2S_3@C core-double shell polyhedron structure from a metal-organic framework. This composite serves as anode materials in SIBs and demonstrates a reversible capacity of 630 mA h g^{-1} at 100 mA g^{-1} after 120 cycles. Consequently, the heterogeneous interface between the two different metal sulfides may generate an internal electric field and provide special channels; thus, the electrochemical performance and structural stability of composites improve. Moreover, Ding's group [19] fabricated a three-dimensional SnS_2 flower/carbon nanotube network that yields a reversible capacity of 460 mA h g^{-1} at 20 mA g^{-1}. Ji's group [18] reported that one-dimensional Sb_2S_3@C rod-based SIBs have a high capacity of 699.1 mA h g^{-1} after 100 cycles at a current density of 100 mA g^{-1}, because of the introduced carbon layer relieving the change in volume.

Electrolytes also play a crucial role in batteries with a stable voltage window and superior electrochemical performance. Many researchers found that the capacity and cycling stability of electrodes in ether-based electrolytes can be improved compared with those in carbonate-based electrolytes [24–27]. Using ether-based electrolytes can induce a thinner and more stable solid electrolyte interphase (SEI) film on the electrode surfaces than using carbonate-based electrolytes because of the lower reduction voltage of ether-based solvents [24]. Thus, choosing the appropriate electrolyte with a stable working voltage is essential for high-performance battery systems.

In this work, hierarchical metallic sulfides of $Sb_2S_3/SnS_2/C$ composites were prepared and used as anodes for SIBs. Different electrolytes were utilized to investigate their effects on the Na-storage performance of electrodes based on $Sb_2S_3/SnS_2/C$ composites. The optimized system of $Sb_2S_3/SnS_2/C$ electrode in a $NaPF_6$-diglyme electrolyte was used for the following in-depth

[1] School of Mathematics and Physics, University of Science and Technology Beijing, Beijing 100083, China
[2] State Key Laboratory for Superlattices and Microstructures, Institute of Semiconductors, Chinese Academy of Sciences, Beijing 100083, China
[*] Corresponding authors (emails: chendi@ustb.edu.cn (Chen D); gzshen@semi.ac.cn (Shen G))

measurements. Our results revealed that the system delivered a high reversible capacity of 642 mA h g^{-1} after 600 cycles at 1 A g^{-1} and a good rate performance of 367.3 mA h g^{-1} at 4 A g^{-1}. With superior electrochemical performance, the system of the Sb_2S_3/SnS_2/C heterojunction in the $NaPF_6$-diglyme electrolyte can be considered a promising candidate for practical application in SIBs.

EXPERIMENTAL SECTION

Material synthesis

Preparation of Sb_2S_3 nanorods

In this work, synthesis was performed in accordance with a previously described method with some modifications [28]. First, 0.596 g of $Sb(CH_3COO)_3$ was dissolved in a mixed solution containing 16 mL of ethanol and 6 mL of glycerol and continuously stirred for 30 min. Then, 0.3 g of thioacetamide (TAA) was added to the above solution under vigorous stirring for another 30 min. The obtained solution was transferred into a 40-mL Teflon autoclave, which was heated to 180°C for 10 h. After being cooled to room temperature, a black product was collected, washed with deionized (DI) water and ethanol several times, and dried in a vacuum oven at 80°C for 12 h.

Preparation of Sb_2S_3/SnS_2 dendritic heterostructures

SnS_2 was prepared in accordance with a previously described procedure [29]. In brief, 0.03 g of the as-prepared Sb_2S_3 precursor and 0.5 g of cetyltrimethylammonium bromide (CTAB) were dispersed in 30 mL of isopropanol under ultrasonic treatment for 1 h. In the following step, 0.2 g of $SnCl_4{\cdot}5H_2O$ was added to the solution and stirred for 30 min. Then, 0.25 g of TAA was placed in the well-dispersed solution. After being stirred evenly, the mixed solution was poured into a 40-mL Teflon autoclave and reacted at 180°C for 6 h. After the reaction was complete, the product was collected and rinsed with DI water and ethanol thrice. The sample was dried in a vacuum oven at 80°C for 12 h.

Fabrication of the Sb_2S_3/SnS_2/C composites

Carbon coating was conducted in a manner similar to a previous report [30]. First, 0.03 g of polyvinylidene fluoride (PVDF) was dissolved in 20 mL of *N*-methyl-2-pyrrolidinone (NMP) to form a homogeneous solution. Then, 0.1 g of the Sb_2S_3/SnS_2 dendritic heterostructure was added to the solution and stirred for 4 h. Subsequently, 20 mL of DI water was injected into the obtained solution with continuous stirring for 1 h. The sample was centrifuged, dried, and calcined at 400°C for 2 h to obtain the Sb_2S_3/SnS_2/C composites. For comparison, Sb_2S_3/C and SnS_2/C compounds were also fabricated using the same procedure.

Characterizations

Crystal texture was examined through X-ray diffraction (XRD) measurement by using a Bruker D8 Advance X-ray diffractometer with radiation from a Cu target (Kα, λ = 0.15406 nm). The morphological characteristics of the samples were explored under a scanning electron microscope (SEM; Zeiss Supra 55) and a transmission electron microscope (TEM; JEOLJEM-2100HT). The chemical constituents of the products were probed with an X-ray photoelectron spectroscopy (XPS) system (Escalab 250-Xi). Thermogravimetric analysis (TGA; NETZSCH STA 449 F3/F5) was performed under the following conditions: temperature range of 25–800°C and a heating rate of 10°C min^{-1} in air.

Electrochemical measurements

The Sb_2S_3/C, SnS_2/C, and Sb_2S_3/SnS_2/C composite electrodes were first prepared by mixing the samples with carbon black and PVDF binder at a weight ratio of 7:2:1 in NMP solvent to fabricate SIBs. Next, the slurries were coated on copper foils and then dried in a vacuum oven at 80°C for 12 h. The mass loading of the materials on the substrate was about 1 mg cm^{-2}. A glass fiber GF/D membrane was used as a separator. Several drops of nanodiamond dispersion with a mass content of 5% were added to modify the GF/D membrane and further dried in a vacuum oven at 60°C for 12 h to improve the electrochemical performance of SIBs. The electrochemical properties of the Sb_2S_3/C, SnS_2/C, and Sb_2S_3/SnS_2/C electrodes were measured in CR2032 half cells with Na chips in the potential range of 0.01–3.0 V. Then, 1 mol L^{-1} $NaPF_6$ in diglyme solvent and 1 mol L^{-1} $NaPF_6$ in ethylene carbonate (EC):dimethyl carbonate (DMC; 1:1 in volume) with 5% fluoroethylene carbonate (FEC) were used as electrolytes. A multichannel battery testing system (Land-CT2001A) was applied to measure galvanostatic charge-discharge (GCD) curves, and a CHI760 electrochemical workstation was employed to test the cyclic voltammetry (CV) curves of the batteries. The electrochemical impedance spectroscopy (EIS) plot in the frequency range of 0.01–10^6 Hz was recorded, and the galvanostatic intermittent titration technique (GITT) was used on an AutoLab (PGSTAT302N) electrochemical analyzer. In GITT, a cell was discharged under a current density of 0.05 A g^{-1} for 5 min and allowed to rest in the voltage range of 0.01–3.0 V for 20 min. A full cell was fabricated using NASICON-type $Na_3V(PO_3)_3N$ coated on Al foil as a cathode. The mass ratio of the anode and the cathode was around 1:8. Furthermore, 1 mol L^{-1} $NaPF_6$ in diglyme solvent and the same separator were used in the full cell. Before the full cell was assembled, the anode was activated in a half cell for three cycles at 0.1 A g^{-1}. The charge-discharge curves and cycling stability of the full cell were examined at the potential of 1–4 V.

RESULTS AND DISCUSSION

The morphological characteristics and microstructures of Sb_2S_3, SnS_2, and Sb_2S_3/SnS_2 heterojunction were observed through SEM and TEM, respectively. Fig. 1a shows the SEM image of the hydrothermally produced Sb_2S_3 nanorods with a diameter of around 100 nm. Numerous SnS_2 nanoplates were assembled to form flower-like structures with a diameter of 3–5 μm (Fig. S1a). Interestingly, the SnS_2 nanoplates could be grown on the Sb_2S_3 nanorod *in situ* by embellishing the Sb_2S_3 precursor with CTAB. Clearly, as an ionic surfactant, CTAB can effectively reduce the surface tension and needs less energy to form new phases. It can also act as a carrier of growth units and influence the growth orientation of materials through its electrostatic and stereochemical effects [31]. In Fig. 1b, dendritic Sb_2S_3/SnS_2 heterostructures with a diameter of ~1 μm were obtained. After these heterostructures were further coated with the carbon layer, their morphological characteristics slightly changed (Fig. S1b). Fig. 1c illustrates the magnified SEM image of the Sb_2S_3/SnS_2/C materials and the nanosheets attached to the nanorod. By comparison, the mixtures of dispersed nanorods and nanoplate-based flower-like structures, not the dendritic heterostructures, were

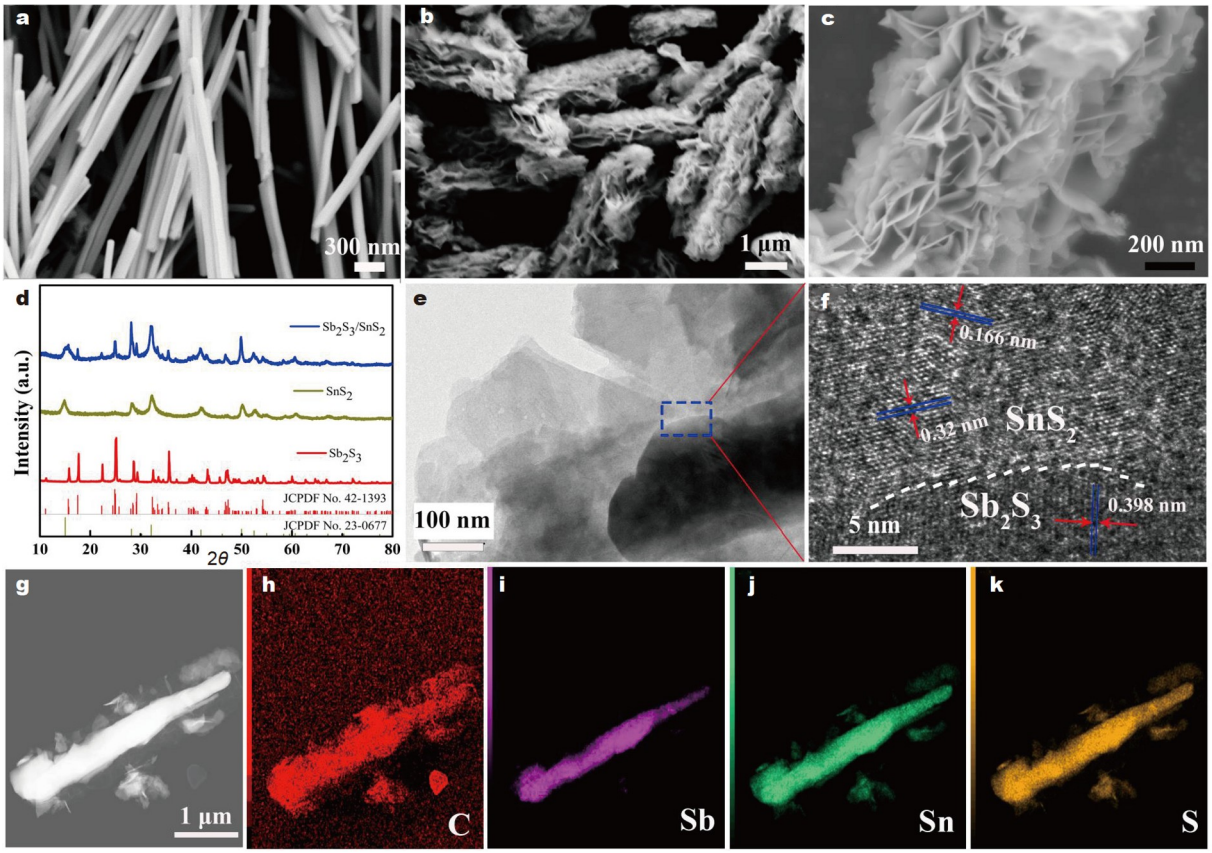

Figure 1 SEM images of (a) Sb_2S_3, (b) Sb_2S_3/SnS_2, and (c) $Sb_2S_3/SnS_2/C$. (d) XRD patterns of Sb_2S_3, SnS_2, and Sb_2S_3/SnS_2. (e, f) TEM and HRTEM images of $Sb_2S_3/SnS_2/C$. (g–k) High-angle annular dark field (HAADF)-HRTEM image of $Sb_2S_3/SnS_2/C$ and the corresponding energy dispersive X-ray spectroscopy (EDS) mappings of C, Sb, Sn, and S.

prepared in the absence of CTAB (Fig. S2).

Fig. 1d presents the XRD patterns of the fabricated Sb_2S_3, SnS_2, and Sb_2S_3/SnS_2 materials. All of the diffractions of Sb_2S_3 and SnS_2 samples were consistent with the standard cards of JCPDS 42-1393 and JCPDS 23-0677, respectively [18,20]. Simultaneously, the XRD results of Sb_2S_3/SnS_2 and $Sb_2S_3/SnS_2/C$ (Fig. S3) had similar diffraction peaks to those of pure Sb_2S_3 and exhibited other strong peaks belonging to SnS_2; therefore, Sb_2S_3 and SnS_2 were present in the heterostructure samples [16]. Fig. 1e depicts the TEM image of the $Sb_2S_3/SnS_2/C$ heterostructures. The black bar denotes Sb_2S_3, and the translucent plates correspond to SnS_2. The selected area electron diffraction (SAED) and high-resolution TEM (HRTEM) images in Fig. S4a reveal that the Sb_2S_3 nanorods were monocrystalline materials with clear lattice fingers of 0.566 and 0.398 nm corresponding to the (020) and (220) crystal faces. The SAED in the inset of Fig. S4b also illustrates the polycrystalline structure of the SnS_2 nanoplate. The HRTEM image in Fig. S4b presents the interplanar distances of 0.320, 0.210, and 0.295 nm, which could be indexed to (100), (102), and (002) lattice planes of SnS_2. Fig. 1f shows the magnified blue marked area in Fig. 1e, where the crystal faces of (100) and (103) of SnS_2 and the (220) of Sb_2S_3 existed. This finding demonstrates that the Sb_2S_3/SnS_2 heterostructure is formed in the interface. Furthermore, the element distributions of the $Sb_2S_3/SnS_2/C$ heterostructure were measured (Fig. 1g–k), and the results showed that C, Sb, Sn, and S were distributed homogeneously in the sample.

The surface chemical compositions of $Sb_2S_3/SnS_2/C$ were examined through XPS. Fig. 2a presents the overall XPS spectrum of the fabricated $Sb_2S_3/SnS_2/C$ with the signals of C, Sb, Sn, and S, signifying the formation of the $Sb_2S_3/SnS_2/C$ composite. High-resolution XPS spectra were obtained to further test the valence states of the elements. The C 1s spectrum in Fig. 2b was fitted into three peaks at 284.6, 285.1, and 289.1 eV, which belong to C–C, C–S, and C=O, respectively [32]. Fig. 2c shows the Sn 3d spectrum with peaks at around 487.0 and 495.4 eV corresponding to Sn $3d_{5/2}$ and Sn $3d_{3/2}$, respectively. The peaks of the Sb 3d spectrum in Fig. 2d centered at 529.9 and 539.3 eV are correlated with Sb $3d_{5/2}$ and Sb $3d_{3/2}$, respectively [33]. The binding energy at 532.4 eV belongs to the O 1s peak, representing surface hydroxyl groups [28]. As shown in Fig. 2e, the S 2p spectrum exhibits the peaks at 161.9 and 163.1 eV, which respond to S^{2-} in S–Sb/S–Sn, respectively. Besides, the peak at 164.9 eV likely corresponds to the covalent bond with carbon [23]. According to the peak areas, the calculated atomic ratios of Sb and Sn were 23 and 77 at%, respectively. The TGA result in Fig. 2f indicates that the contents of C, Sb_2S_3, and SnS_2 were 9.9%, 19.6%, and 70.5%, respectively.

CR2032 coin cells were assembled by using the $Sb_2S_3/SnS_2/C$ heterostructure, Sb_2S_3/C, SnS_2/C, and the samples prepared without CTAB as working electrodes and Na chip as a reference electrode to investigate the sodium-ion storage performance of the as-prepared samples. The SIBs with $NaPF_6$-diglyme and $NaPF_6$-EC/DMC electrolytes were used to compare the electrochemical performance. The CV curves of the electrodes in 1 mol L^{-1} $NaPF_6$-diglyme electrolyte (Fig. 3a and Fig. S5) were

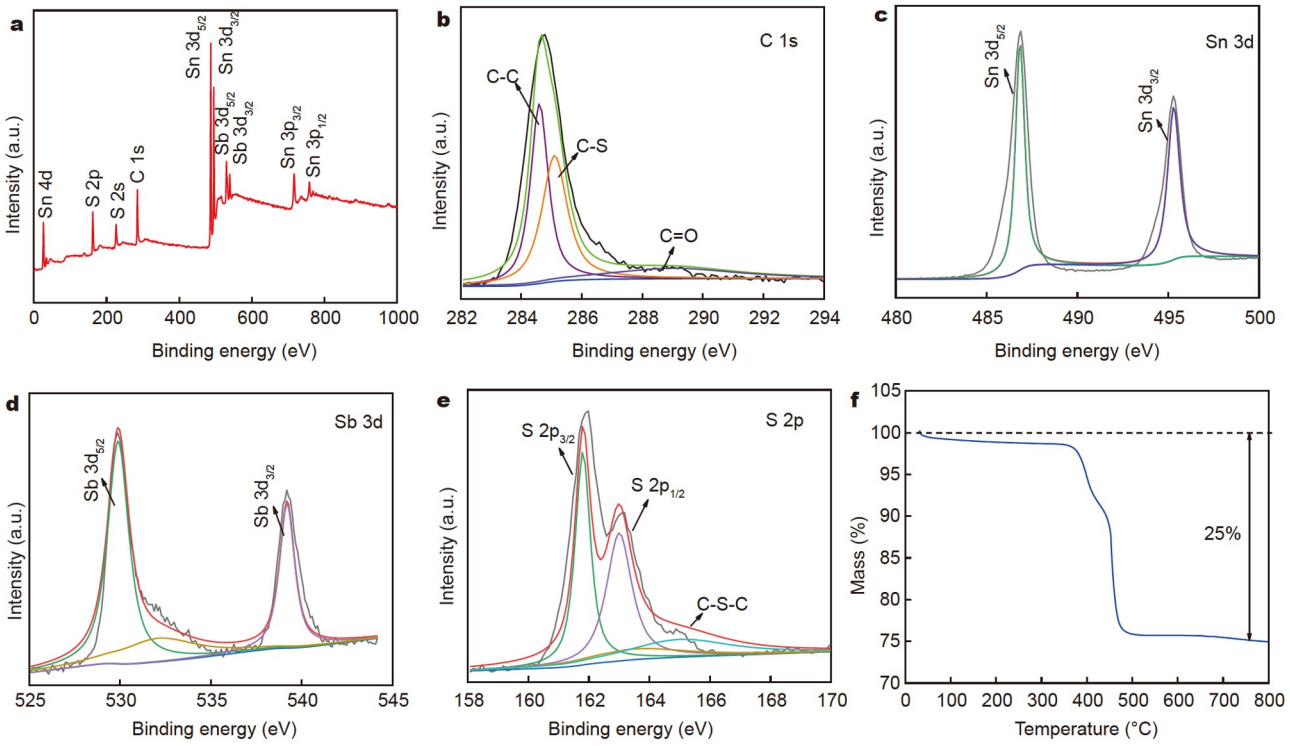

Figure 2 (a) XPS spectrum of $Sb_2S_3/SnS_2/C$. (b–e) High-resolution XPS spectra of C 1s, Sn 3d, Sb 3d, and S 2p. (f) TGA curve of $Sb_2S_3/SnS_2/C$.

tested in the potential range of 0.01–3.0 V at a scan rate of 1 mV s^{-1}. The capacitance of $Sb_2S_3/SnS_2/C$ (1453 F g^{-1}, 1090 mA h g^{-1}) in the $NaPF_6$-diglyme electrolyte calculated from the CV curve was higher than those of Sb_2S_3/C (726 F g^{-1}, 545 mA h g^{-1}), SnS_2/C (953 F g^{-1}, 715 mA h g^{-1}), and their mixture (676 F g^{-1}, 507 mA h g^{-1}). Similarly, Fig. 3b shows that the capacitance of $Sb_2S_3/SnS_2/C$ in the $NaPF_6$-EC/DMC electrolyte was 531 F g^{-1} (398 mA h g^{-1}), which was superior to those of Sb_2S_3/C (173 F g^{-1}, 130 mA h g^{-1}), SnS_2/C (174 F g^{-1}, 131 mA h g^{-1}), and their mixture (125 F g^{-1}, 94 mA h g^{-1}). Thus, the system of $Sb_2S_3/SnS_2/C$ heterojunction composites in the $NaPF_6$-diglyme electrolyte was chosen for the following in-depth measurements. According to previous reports, a nanodiamond is characterized by a large specific surface area and chemical inertness; as such, ions can easily adsorb on its surface and form a stable SEI film, thus reducing the occurrence of side reactions [34–37]. Here, the nanodiamond dispersion with a mass content of 5% was used to modify the separator, which not only helped increase the amount of electrolyte adsorbed but also maintained the integrity of the separator. Fig. S6 shows the results of the CV tests of the half cells using the $Sb_2S_3/SnS_2/C$ electrode in the $NaPF_6$-diglyme electrolyte with/without nanodiamond-modified separators. After calculation, the capacitance of the battery with the nanodiamond-modified separator (1453 F g^{-1}, 1090 mA h g^{-1}) was higher than that without modification (1033 F g^{-1}, 775 mA h g^{-1}). Therefore, the embellishment with nanodiamonds helps improve the electrochemical performance.

A series of comparative tests were carried out to examine the Na-storage performance of the electrode based on $Sb_2S_3/SnS_2/C$ composites in different electrolytes. Fig. 4a shows the CV curves of the $Sb_2S_3/SnS_2/C$ electrode in two kinds of electrolytes at a sweep rate of 1 mV s^{-1} with the potential range of 0.01–3.0 V. The integral area of the $Sb_2S_3/SnS_2/C$ electrode in the $NaPF_6$-diglyme electrolyte was larger than that in the $NaPF_6$-EC/DMC electrolyte (Fig. 3). This result implies that using ether-based electrolytes could help enhance electrochemical performance. Fig. S7 illustrates the GCD profiles of the $Sb_2S_3/SnS_2/C$ electrode for the first two cycles at 1 A g^{-1} in the two kinds of electrolytes. Based on the profiles, the histogram of the charging and discharging capacities is ploted (Fig. 4b). The initial discharging and charging capacities of the $Sb_2S_3/SnS_2/C$ electrode in the $NaPF_6$-diglyme electrolyte were 924.3 and 540.7 mA h g^{-1} with a Coulombic efficiency of 58%, respectively. In the second cycle, a Coulombic efficiency of 83.7% could be recovered. By comparison, the original discharging and charging capacities of the $Sb_2S_3/SnS_2/C$ electrode in the $NaPF_6$-EC/DMC electrolyte were lower, i.e., 529.2 and 222.1 mA h g^{-1}, with a Coulombic efficiency of 41.9%. The Coulombic efficiency of the second cycle was restored to 61.7%. Consequently, the irreversible capacity loss in the $NaPF_6$-EC/DMC electrolyte was higher than that in the diglyme solvent. Fig. 4c displays the EIS of the devices in different solvents with frequencies of 10^6 to 0.01 Hz. The charge transfer resistance of the $Sb_2S_3/SnS_2/C$ electrode in the $NaPF_6$-EC/DMC electrolyte (632 Ω) was larger than that in the $NaPF_6$-diglyme electrolyte (101 Ω). According to the report, the reduction voltage of the EC/DMC solvent is higher than that of the diglyme solvent, and the former is more easily reduced on the surface of the electrode than the latter [24]. Hence, electrolyte decomposition can lead to SEI film formation, causing the charge transfer resistance to increase. Fig. S8 presents the corresponding equivalent circuit diagram of the fabricated batteries, where R_s represents the ohmic electrolyte resistance, R_p denotes the charge transfer resistance, CPE expresses constant phase elements, and W depicts the ion-diffusion resistance [38]. Additionally, the GITT measurement within the potential range

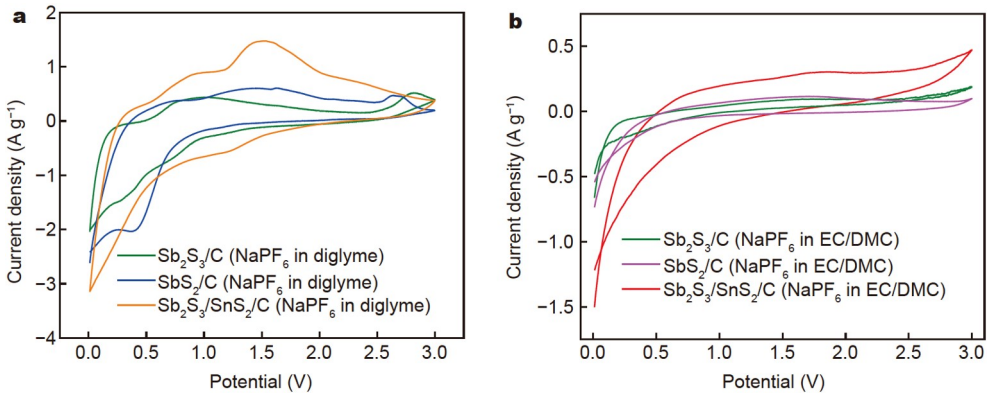

Figure 3 CV curves of sodium-ion half cells based on Sb_2S_3/C, SnS_2/C, and Sb_2S_3/SnS_2/C electrodes at a scan rate of 1 mV s^{-1} in (a) $NaPF_6$-diglyme electrolyte and (b) $NaPF_6$-EC/DMC electrolyte.

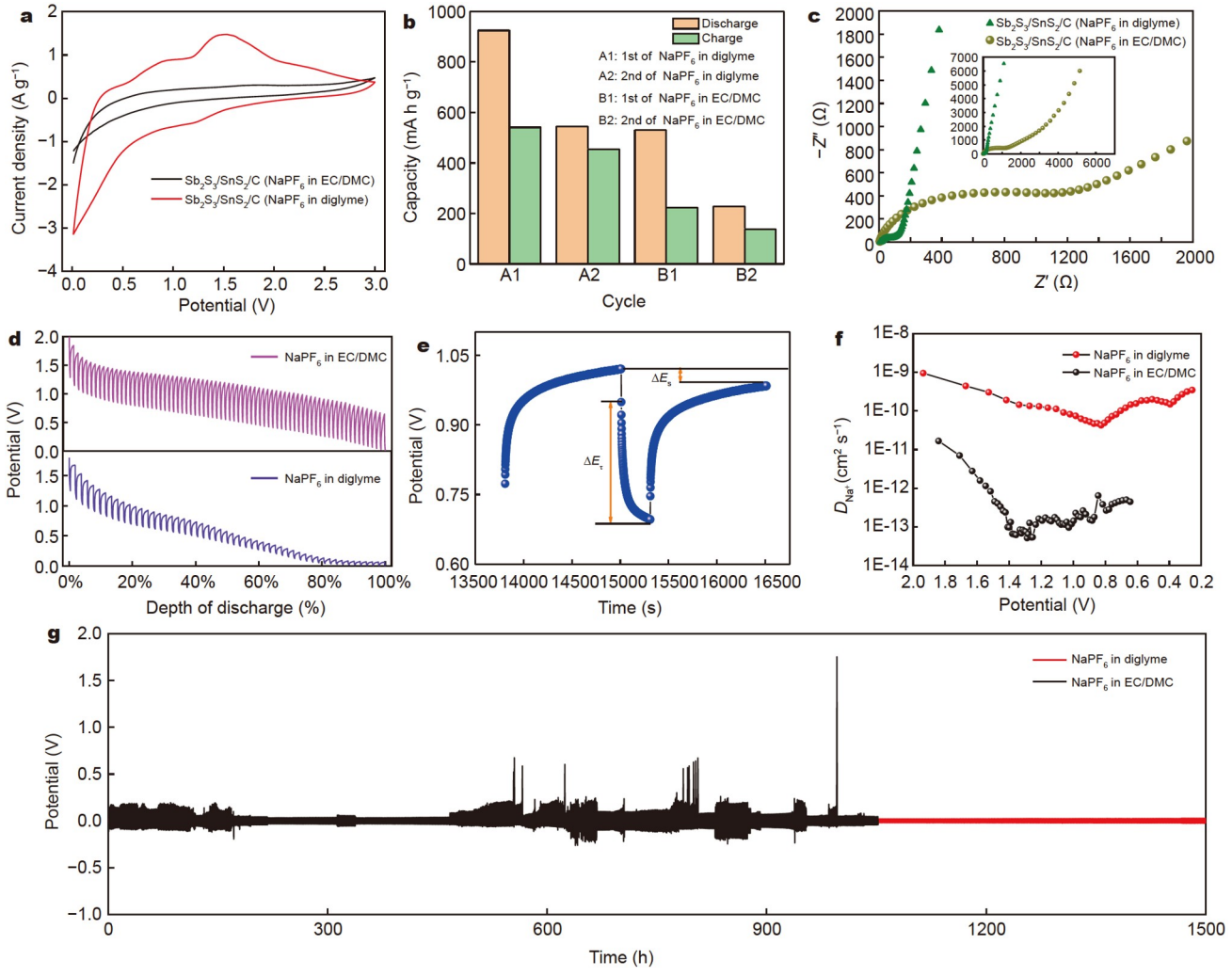

Figure 4 Comparison of the electrochemical properties of the Sb_2S_3/SnS_2/C electrode in $NaPF_6$-diglyme and $NaPF_6$-EC/DMC electrolytes. (a) CV curves at a sweep rate of 1 mV s^{-1}. (b) Histogram of the charging/discharging capacities of the first two cycles at a current density of 1 A g^{-1}. (c) Magnified Nyquist plots. Inset is the Nyquist impedance plot of the devices in different electrolytes. (d) Discharging curves of the GITT profiles. (e) Detailed change in the potential of the Sb_2S_3/SnS_2/C electrode in $NaPF_6$-diglyme electrolyte during a single step of pulse and relaxation. (f) Diffusion coefficients of Na^+ during the discharging process. (g) Charge-discharge curves of symmetrical Na//Na cells with two different electrolytes at 0.3 mA cm^{-2}.

of 0.01–3.0 V was conducted to investigate the sodium-ion storage kinetics in the two kinds of electrolytes (Fig. 4d). In the single-step GITT test, the cell was discharged at 0.05 A g^{-1} for 5 min and subjected to relaxation for 20 min to achieve a steady-state potential (Fig. 4e and Fig. S9) according to the calculation formula [33]:

$$D_{Na^+} = \frac{4}{\pi\tau}\left(\frac{m_B V_M}{M_B S}\right)^2\left(\frac{\Delta E_S}{\Delta E_\tau}\right)^2,$$

where m_B, V_M, and M_B are the mass, molar volume, and molar weight of the active materials, respectively; τ is the pulse time; S is the surface area of electrodes; ΔE_s and ΔE_τ are the potential drops between two adjacent steady states and the voltage change after subtracting the *IR* drop in a single titration. D_{Na^+} of the Sb_2S_3/SnS_2/C electrode in the $NaPF_6$-diglyme electrolyte was in the range of 4.3×10^{-11} to 9.5×10^{-10} cm^2 s^{-1} (Fig. 4f), which was higher than that in the $NaPF_6$-EC/DMC electrolyte (5.1×10^{-14} to 1.6×10^{-11} cm^2 s^{-1}), because ether-based electrolytes can effectively accelerate sodium-ion diffusion and electron transport [39]. Furthermore, the long-term cycling stability and compatibility of the two kinds of electrolytes with Na metal were explored in symmetrical Na//Na cells. Fig. 4g shows the charging and discharging curves of the devices at the current density of 0.3 mA cm^{-2}. In comparison with Na/$NaPF_6$-(EC/DMC)/Na, the voltage of the Na/$NaPF_6$-Diglyme/Na device appeared relatively stable at 25 mV for 1500 h; as such, it contributed to the increased ionic conductivity and electrochemical stability of the $NaPF_6$-diglyme electrolyte [40]. Therefore, the $NaPF_6$-diglyme electrolyte system can be used to improve the electrochemical performance of the Sb_2S_3/SnS_2/C electrode effectively.

The electrochemical properties of Sb_2S_3/C, SnS_2/C, and Sb_2S_3/SnS_2/C electrode materials in the $NaPF_6$-diglyme electrolyte were tested to further illustrate the advantages of the Sb_2S_3/SnS_2/C heterojunction material for Na-ion storage. Fig. 5a shows the charging and discharging capacities of Sb_2S_3/C, SnS_2/C, and Sb_2S_3/SnS_2/C electrodes at 1 A g^{-1} for the first two cycles. The maximum discharging and charging capacities of the Sb_2S_3/SnS_2/C electrode were 924.3 and 540.7 mA h g^{-1} with the first Coulombic efficiency of 58%, respectively. In the second cycle, the Coulombic efficiency could be recovered to 83.7%. By contrast, the original discharging/charging capacities of the Sb_2S_3/C and SnS_2/C electrodes in the same ether-based electrolyte were 943.1/360.9 and 806.3/218.4 mA h g^{-1}, respectively, and their initial Coulombic efficiencies were 38.3% and 27.1%, respectively. In the second cycle, the Coulombic efficiencies returned to 43.1% and 76.3%, respectively. Thus, the capacity retention of the Sb_2S_3/SnS_2/C heterostructure material is much higher than those of Sb_2S_3/C and SnS_2/C. Fig. 5b shows the Nyquist plots of the Sb_2S_3/C, SnS_2/C, and Sb_2S_3/SnS_2/C electrodes. The charge transfer resistance of Sb_2S_3/SnS_2/C (101 Ω) was lower than those of the Sb_2S_3/C (196 Ω) and SnS_2/C electrodes (185 Ω), because of the heterogeneous structure, which facilitates the charge transfer and ion diffusion [21]. D_{Na^+} of Sb_2S_3/SnS_2/C (4.3×10^{-11}–9.5×10^{-10} cm^2 s^{-1}) was much higher than those of Sb_2S_3/C (1.0×10^{-13}–4.7×10^{-10} cm^2 s^{-1}) and SnS_2/C (4.5×10^{-13}–5.1×10^{-10} cm^2 s^{-1}) electrodes in the $NaPF_6$-diglyme electrolyte (Fig. 5c). Therefore, heterogeneous structures contribute to the ionic diffusion.

The long-term cycling stability of the Sb_2S_3/C, SnS_2/C, and Sb_2S_3/SnS_2/C electrodes was examined at the current density of

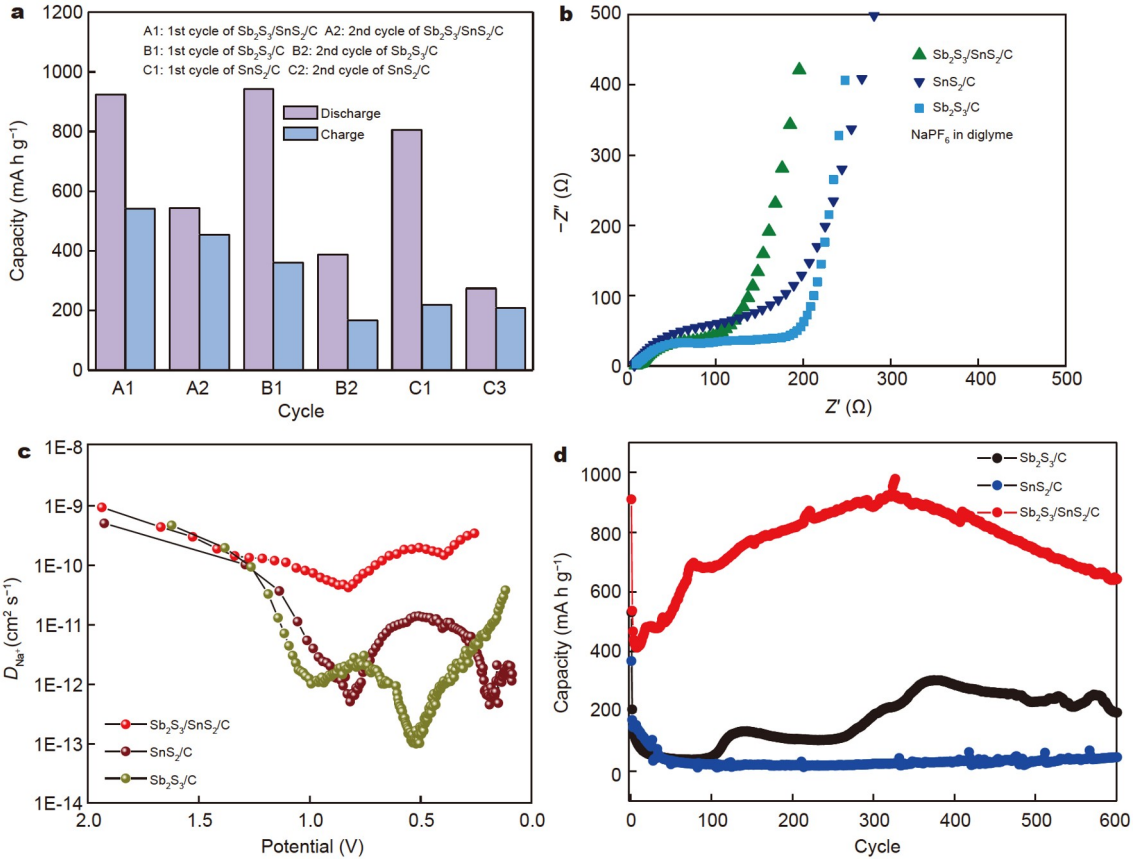

Figure 5 Comparison of the electrochemical performance of Sb_2S_3/C, SnS_2/C, and Sb_2S_3/SnS_2/C electrodes in the $NaPF_6$-diglyme electrolyte. (a) Charge and discharge capacities in the first two cycles at a current density of 1 A g^{-1}. (b) Nyquist plots. (c) Diffusion coefficients of Na^+ during the discharging process. (d) Cycling stability at a current density of 1 A g^{-1}.

1 A g^{-1} (Fig. 5d). The capacity of the $Sb_2S_3/SnS_2/C$ electrode decreased in the first 10 cycles. In the next 300 cycles, the capacity increased until it reached 920 mA h g^{-1}. In the following cycles, the electrochemical performance gradually decreased, and the final reversible capacity was 642 mA h g^{-1} at the 600th cycle. Therefore, the electrochemical performance and lifespan improved compared with those of previous results [17,20]. This remarkable fluctuation could be attributed to the insufficient active surface area in a pristine state. As the reaction proceeded, more electrolytes on the surface penetrated the materials, and more active materials participated in electrochemical reactions; consequently, capacity rapidly increased. In addition, sulfides tended to expand during electrochemical reactions. The decreased capacity is possibly caused by the structural pulverization and incomplete conversion during the cycling process [41,42]. A roughly similar trend was observed in the Sb_2S_3/C electrode, whose capacity gradually decreased in the first 100 cycles, increased in the next 250 cycles, and finally decreased to 196 mA h g^{-1}. For the SnS_2/C electrode, the capacity was severely reduced to 100 mA h g^{-1} after 20 cycles. Therefore, the electrochemical performance of the $Sb_2S_3/SnS_2/C$ electrode material is relatively better than that of the other electrodes. Transition metal composites usually experience an increase in capacity during cycles because of the activation of electrode materials and the reversible formation of organic polymers through electrolyte degradation [25,43–46].

The sodium-ion storage behavior of the $Sb_2S_3/SnS_2/C$ materials in the $NaPF_6$-diglyme electrolyte was further investigated. Fig. 6a shows the CV curves of the half cell for the first three cycles at a scan rate of 1 mV s^{-1}. During the first cathodic process, the sharp peaks at about 1.72 and 1.45 V correspond to Na^+ intercalation in SnS_2 layers to form $NaSnS_2$ [16,20,33,47,48]:

$SnS_2 + Na^+ + e^- \rightarrow NaSnS_2$.

The broad reduction peak ranging from 1.3 to 0.86 V is attributed to the overlapping conversion reactions of Sb_2S_3 and SnS_2 [17–20,22,23,33,49]:

$Sb_2S_3 + 6Na^+ + 6e^- \rightarrow 2Sb + 3Na_2S$,

$NaSnS_2 + 3Na^+ + 3e^- \rightarrow Sn + 2Na_2S$.

Another long slope from 0.65 and 0.3 V is ascribed to the alloying reactions of Sb and Sn [16–18,20,48–50]. Besides, an irreversible SEI layer is formed in this region [17,18]:

$2Sb + 6Na^+ + 6e^- \rightarrow 2Na_3Sb$,

$Sn + 3.75Na^+ + 3.75e^- \rightarrow Na_{3.75}Sn$.

In the anodic scan, the oxidation peaks at 0.3 and 0.76 V are related to the desodiation of $Na_{3.75}Sn$ and Na_3Sb, respectively [17,18,20,23,48,49]. The broad anodic peak centered at 1.4 V is attributed to the reformation of Sb_2S_3 and $NaSnS_2$. An indistinct peak concentrated at 2.2 V is assigned to the sodium-ion extracted from $NaSnS_2$ [48]. In the subsequent cycles, the location of the peaks slightly changed, possibly because of the SEI film formation with irreversible side reactions [18]. Fig. 6b displays the GCD curves of the 1st, 2nd, 3rd, 100th, 200th, and 300th cycles at 1 A g^{-1}. In the first few anodic cycles, the activation barrier for desodiation was high. As the materials expanded in volume and the particles size became smaller in the subsequent cycles, the kinetic barrier decreased, indicating that the reaction kinetics accelerated. Therefore, the initial anodic reaction platform decreased below 2.0 V in the 100th, 200th, and 300th cycles [51,52].

The first discharging and charging capacities of the $Sb_2S_3/SnS_2/C$ electrode were 924.3 and 540.7 mA h g^{-1}, respectively. Simultaneously, the discharging capacities of the 100th, 200th, and 300th cycles (680, 814.3, and 882.1 mA h g^{-1}, respectively) were much higher than those of the 2nd and 3rd cycles (535 and 465.7 mA h g^{-1}, respectively), which were consistent with the results shown in Fig. 5d. Fig. 6c illustrates the rate property of $Sb_2S_3/SnS_2/C$ in the $NaPF_6$-diglyme electrolyte with current densities of 0.1–4.0 A g^{-1}. The average capacities of 929.8, 684.9,

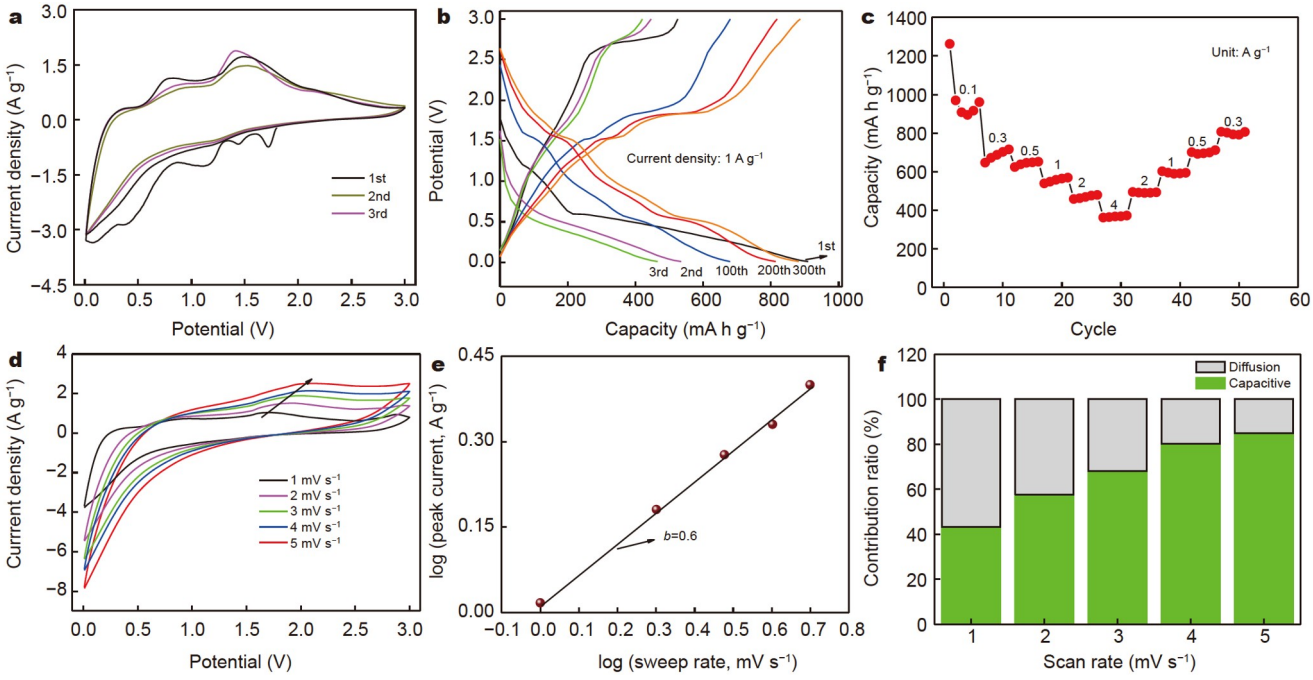

Figure 6 Sodium-ion storage performance of the $Sb_2S_3/SnS_2/C$ electrode in the $NaPF_6$-diglyme electrolyte. (a) CV curves of the first three cycles at a sweep rate of 1 mV s^{-1}. (b) GCD profiles at the current density of 1 A g^{-1}. (c) Rate capability. (d–f) CV curves, peak current, and diffusion and capacitive contributions at different scan rates of 1–5 mV s^{-1}.

641.9, 555.8, 469.1, and 367.3 mA h g^{-1} at 0.1, 0.3, 0.5, 1.0, 2.0, and 4.0 A g^{-1} were achieved, respectively. When the current density was returned to 0.3 A g^{-1}, an improved specific capacity of 800.2 mA h g^{-1} could be obtained because of the activation process, demonstrating the decent rate performance of the Sb_2S_3/SnS_2/C materials. In addition, the CV curves at various scan rates of 1–5 mV s^{-1} were obtained to reveal the possible reason for superior rate properties (Fig. 6d). Because Sb_2S_3 and SnS_2 are pseudocapacitance materials, the electrochemical capacity generally included the diffusion-controlled value and the surface capacitive contribution according to the following computational formula:

$i = av^b$,

where a and b are two adjustable parameters, i is the current (A g^{-1}), and v is the scan rate (mV s^{-1}) [53]. Specifically, the b-values of 0.5 and 1 illustrate that the charge storage is dominated by the diffusion-controlled process and surface capacitive contribution, respectively. In Fig. 6e, the b-value of the anodic peak was 0.6, suggesting that the capacitive contribution and diffusion-controlled process coexisted. Moreover, the surface capacitive contribution can be inferred by the following formula [54]:

$i = k_1v + k_2v^{1/2}$,

where k_1v and $k_2v^{1/2}$ are the values of the surface capacitive and diffusion-controlled contributions at the given specific voltage, respectively. Thus, the capacitive contribution profile of the Sb_2S_3/SnS_2/C electrode was 43.2% at the scan rate of 1 mV s^{-1} (Fig. S10). Encouragingly, the surface capacitive contribution improved as the scan rate increased (Fig. 6f), which could reach 84.8% at 5 mV s^{-1}. The high proportion of capacitive contribution could help enhance the rate performance of electrode materials. In addition, a Na-ion full cell was assembled by pairing with a $Na_3V(PO_3)_3N$ cathode [55]. Fig. S11 shows the electrochemical performance of the full cell. A typical discharge curve of the Na-ion full cell displays a specific capacity of 348 mA h g^{-1} at 0.1 A g^{-1} under the potential of 1–4 V (based on the weight of the anode). Moreover, a good capacity retention of 81% was retained after 40 cycles at 0.1 A g^{-1}. Simultaneously, the energy and power densities of the full cell were calculated using the formulas described in previous reports [56]. The maximum energy density was 120 W h kg^{-1} based on the total mass of anode and cathode materials.

CONCLUSION

In summary, a one-dimensional Sb_2S_3/SnS_2/C heterostructure was successfully prepared by directly growing SnS_2 nanoplates on Sb_2S_3 nanorods and then coating their surface with a carbon layer. The electrochemical performance of the obtained heterostructure is superior to that of individual Sb_2S_3/C and SnS_2/C electrodes. The sodium-ion storage property improves because (i) the Sb_2S_3/SnS_2/C composites with a special heterogeneous structure could induce an electric field within the nanocrystals, consequently decreasing their ion-diffusion resistance and promoting ion and electron transport. (ii) The carbon coating not only enhances electrical conductivity but also alleviates volume expansion in the sodiation/desodiation process. (iii) The ether-based electrolyte with lower reduction voltage can facilitate the formation of a thinner and more stable SEI film on the electrode surface than that in a carbonate-based electrolyte. Consequently, the charge transfer resistance decreases. Thus, the following electrochemical properties of the Sb_2S_3/SnS_2/C electrode are obtained: a reversible capacity of 642 mA h g^{-1} at 1 A g^{-1} after 600 times cycles and a good rate performance of 367.3 mA h g^{-1} at an increased current density of 4 A g^{-1}. Indeed, Sb_2S_3/SnS_2/C heterostructures are competitive anode materials for SIBs.

Received 13 October 2021; accepted 14 December 2021; published online 14 February 2022

1 Wang Y, Yang Q, Zhao Y, *et al.* Recent advances in electrode fabrication for flexible energy-storage devices. Adv Mater Technol, 2019, 4: 1900083
2 Wang G, He P, Fan LZ. Asymmetric polymer electrolyte constructed by metal-organic framework for solid-state, dendrite-free lithium metal battery. Adv Funct Mater, 2021, 31: 2007198
3 Lee J, Wang C, Malik R, *et al.* Determining the criticality of Li-excess for disordered-rocksalt Li-ion battery cathodes. Adv Energy Mater, 2021, 11: 2100204
4 Lin J, Zeng C, Lin X, *et al.* Metal-organic framework-derived hierarchical MnO/Co with oxygen vacancies toward elevated-temperature Li-ion battery. ACS Nano, 2021, 15: 4594–4607
5 Zuo W, Li R, Zhou C, *et al.* Battery-supercapacitor hybrid devices: Recent progress and future prospects. Adv Sci, 2017, 4: 1600539
6 Wang H, Zhu C, Chao D, *et al.* Nonaqueous hybrid lithium-ion and sodium-ion capacitors. Adv Mater, 2017, 29: 1702093
7 Choi C, Ashby DS, Butts DM, *et al.* Achieving high energy density and high power density with pseudocapacitive materials. Nat Rev Mater, 2020, 5: 5–19
8 Zhang L, Wei Q, Sun D, *et al.* Conversion reaction of vanadium sulfide electrode in the lithium-ion cell: Reversible or not reversible? Nano Energy, 2018, 51: 391–399
9 Wei Q, Jiang Y, Qian X, *et al.* Sodium ion capacitor using pseudocapacitive layered ferric vanadate nanosheets cathode. iScience, 2018, 6: 212–221
10 Xia X, Chao D, Zhang Y, *et al.* Generic synthesis of carbon nanotube branches on metal oxide arrays exhibiting stable high-rate and long-cycle sodium-ion storage. Small, 2016, 12: 3048–3058
11 Kim MS, Lim E, Kim S, *et al.* General synthesis of N-doped macroporous graphene-encapsulated mesoporous metal oxides and their application as new anode materials for sodium-ion hybrid supercapacitors. Adv Funct Mater, 2017, 27: 1603921
12 Kumaresan TK, Masilamani SA, Raman K, *et al.* High performance sodium-ion battery anode using biomass derived hard carbon with engineered defective sites. Electrochim Acta, 2021, 368: 137574
13 Liu M, Zhang J, Guo S, *et al.* Chemically presodiated hard carbon anodes with enhanced initial Coulombic efficiencies for high-energy sodium ion batteries. ACS Appl Mater Interfaces, 2020, 12: 17620–17627
14 Lao M, Zhang Y, Luo W, *et al.* Alloy-based anode materials toward advanced sodium-ion batteries. Adv Mater, 2017, 29: 1700622
15 Xiao Y, Lee SH, Sun YK. The application of metal sulfides in sodium ion batteries. Adv Energy Mater, 2016, 7: 1601329
16 Xie X, Su D, Chen S, *et al.* SnS_2 nanoplatelet@graphene nanocomposites as high-capacity anode materials for sodium-ion batteries. Chem Asian J, 2014, 9: 1611–1617
17 Zhu Y, Nie P, Shen L, *et al.* High rate capability and superior cycle stability of a flower-like Sb_2S_3 anode for high-capacity sodium ion batteries. Nanoscale, 2015, 7: 3309–3315
18 Hou H, Jing M, Huang Z, *et al.* One-dimensional rod-like Sb_2S_3-based anode for high-performance sodium-ion batteries. ACS Appl Mater Interfaces, 2015, 7: 19362–19369
19 Ren Y, Wang J, Huang X, *et al.* Three-dimensional SnS_2 flowers/carbon nanotubes network: Extraordinary rate capacity for sodium-ion battery. Mater Lett, 2017, 186: 57–61
20 Wang J, Luo C, Mao J, *et al.* Solid-state fabrication of SnS_2/C nanospheres for high-performance sodium ion battery anode. ACS Appl Mater Interfaces, 2015, 7: 11476–11481
21 Cao L, Gao X, Zhang B, *et al.* Bimetallic sulfide Sb_2S_3@FeS_2 hollow nanorods as high-performance anode materials for sodium-ion batteries. ACS Nano, 2020, 14: 3610–3620
22 Zhang Z, Zhao J, Xu M, *et al.* Facile synthesis of Sb_2S_3/MoS_2 hetero-

structure as anode material for sodium-ion batteries. Nanotechnology, 2018, 29: 335401
23 Dong S, Li C, Ge X, *et al.* ZnS-Sb_2S_3@C core-double shell polyhedron structure derived from metal-organic framework as anodes for high performance sodium ion batteries. ACS Nano, 2017, 11: 6474–6482
24 Zhang J, Wang DW, Lv W, *et al.* Achieving superb sodium storage performance on carbon anodes through an ether-derived solid electrolyte interphase. Energy Environ Sci, 2017, 10: 370–376
25 Wu J, Liu J, Cui J, *et al.* Dual-phase MoS_2 as a high-performance sodium-ion battery anode. J Mater Chem A, 2020, 8: 2114–2122
26 Wan Y, Song K, Chen W, *et al.* Ultra-high initial Coulombic efficiency induced by interface engineering enables rapid, stable sodium storage. Angew Chem Int Ed, 2021, 60: 11481–11486
27 Zhang M, Li Y, Wu F, *et al.* Boosting the ultrahigh initial coulombic efficiency of porous carbon anodes for sodium-ion batteries *via in situ* fabrication of a passivation interface. J Mater Chem A, 2021, 9: 10780–10788
28 Sahoo RK, Singh S, Yun JM, *et al.* Sb_2S_3 nanoparticles anchored or encapsulated by the sulfur-doped carbon sheet for high-performance supercapacitors. ACS Appl Mater Interfaces, 2019, 11: 33966–33977
29 Wang M, Fan L, Wu X, *et al.* SnS_2/SnO_2 heterostructures towards enhanced electrochemical performance of lithium-sulfur batteries. Chem Eur J, 2019, 25: 5416–5421
30 Ge P, Zhang L, Zhao W, *et al.* Interfacial bonding of metal-sulfides with double carbon for improving reversibility of advanced alkali-ion batteries. Adv Funct Mater, 2020, 30: 1910599
31 Sun XM, Chen X, Deng ZX, *et al.* A CTAB-assisted hydrothermal orientation growth of ZnO nanorods. Mater Chem Phys, 2002, 78: 99–104
32 Liang H, Ni J, Li L. Bio-inspired engineering of Bi_2S_3-PPy yolk-shell composite for highly durable lithium and sodium storage. Nano Energy, 2017, 33: 213–220
33 Wang S, Liu S, Li X, *et al.* SnS_2/Sb_2S_3 heterostructures anchored on reduced graphene oxide nanosheets with superior rate capability for sodium-ion batteries. Chem Eur J, 2018, 24: 3873–3881
34 Cheng XB, Zhao MQ, Chen C, *et al.* Nanodiamonds suppress the growth of lithium dendrites. Nat Commun, 2017, 8: 336
35 Polino G, Scaramella A, Manca V, *et al.* Nanodiamond-based separators for supercapacitors realized on paper substrates. Energy Technol, 2020, 8: 1901233
36 Song Y, Li H, Wang L, *et al.* Nanodiamonds: A critical component of anodes for high performance lithium-ion batteries. Chem Commun, 2016, 52: 10497–10500
37 Postnov VN, Mel'nikova NA, Shul'meister GA, *et al.* Nafion- and aquivion-based nanocomposites containing detonation nanodiamonds. Russ J Gen Chem, 2017, 87: 2754–2755
38 Jia R, Du H, Zhang X, *et al.* Stretchable and compressible supercapacitor with polyaniline on hydrogel electrolyte. J Electrochem Soc, 2018, 165: A3792–A3798
39 Su D, Kretschmer K, Wang G. Improved electrochemical performance of Na-ion batteries in ether-based electrolytes: A case study of ZnS nanospheres. Adv Energy Mater, 2016, 6: 1501785
40 Li D, Chen L, Wang T, *et al.* 3D fiber-network-reinforced bicontinuous composite solid electrolyte for dendrite-free lithium metal batteries. ACS Appl Mater Interfaces, 2018, 10: 7069–7078
41 Wu C, Wu ZG, Zhang X, *et al.* Insight into the origin of capacity fluctuation of $Na_2Ti_6O_{13}$ anode in sodium ion batteries. ACS Appl Mater Interfaces, 2017, 9: 43596–43602
42 Park JY, Kim SJ, Yim K, *et al.* Pulverization-tolerance and capacity recovery of copper sulfide for high-performance sodium storage. Adv Sci, 2019, 6: 1900264
43 Jiao Y, Mukhopadhyay A, Ma Y, *et al.* Ion transport nanotube assembled with vertically aligned metallic MoS_2 for high rate lithium-ion batteries. Adv Energy Mater, 2018, 8: 1702779
44 Xue H, Yu DYW, Qing J, *et al.* Pyrite FeS_2 microspheres wrapped by reduced graphene oxide as high-performance lithium-ion battery anodes. J Mater Chem A, 2015, 3: 7945–7949
45 Pan L, Zhu XD, Xie XM, *et al.* Smart hybridization of TiO_2 nanorods and Fe_3O_4 nanoparticles with pristine graphene nanosheets: Hierarchically nanoengineered ternary heterostructures for high-rate lithium storage. Adv Funct Mater, 2015, 25: 3341–3350
46 Han W, Qin X, Wu J, *et al.* Electrosprayed porous Fe_3O_4/carbon microspheres as anode materials for high-performance lithium-ion batteries. Nano Res, 2018, 11: 892–904
47 Zhang Y, Zhu P, Huang L, *et al.* Few-layered SnS_2 on few-layered reduced graphene oxide as Na-ion battery anode with ultralong cycle life and superior rate capability. Adv Funct Mater, 2015, 25: 481–489
48 Fan L, Li X, Song X, *et al.* Promising dual-doped graphene aerogel/SnS_2 nanocrystal building high performance sodium ion batteries. ACS Appl Mater Interfaces, 2018, 10: 2637–2648
49 Yu DYW, Prikhodchenko PV, Mason CW, *et al.* High-capacity antimony sulphide nanoparticle-decorated graphene composite as anode for sodium-ion batteries. Nat Commun, 2013, 4: 2922
50 Thangavel R, Pandian AS, Ramasamy HV, *et al.* Rapidly synthesized, few-layered pseudocapacitive SnS_2 anode for high-power sodium ion batteries. ACS Appl Mater Interfaces, 2017, 9: 40187–40196
51 Lee M, Hong J, Lopez J, *et al.* High-performance sodium-organic battery by realizing four-sodium storage in disodium rhodizonate. Nat Energy, 2017, 2: 861–868
52 Liu Q, Deng W, Sun CF. A potassium-tellurium battery. Energy Storage Mater, 2020, 28: 10–16
53 Wang J, Polleux J, Lim J, *et al.* Pseudocapacitive contributions to electrochemical energy storage in TiO_2 (anatase) nanoparticles. J Phys Chem C, 2007, 111: 14925–14931
54 Cai P, Zou K, Zou G, *et al.* Quinone/ester-based oxygen functional group-incorporated full carbon Li-ion capacitor for enhanced performance. Nanoscale, 2020, 12: 3677–3685
55 Chen M, Hua W, Xiao J, *et al.* Development and investigation of a NASICON-type high-voltage cathode material for high-power sodium-ion batteries. Angew Chem, 2020, 132: 2470–2477
56 Dong X, Chen L, Su X, *et al.* Flexible aqueous lithium-ion battery with high safety and large volumetric energy density. Angew Chem Int Ed, 2016, 55: 7474–7477

Acknowledgements This work was supported by the National Natural Science Foundation of China (51972025).

Author contributions The paper was written through the contributions of all authors. All authors have given approval to the final version of the paper.

Conflict of interest The authors declare that they have no conflict of interest.

Supplementary information Supporting data are available in the online version of this paper.

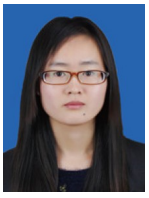

Rui Jia received her BE degree in 2015 from Huaqiao University and ME degree in 2018 from Qingdao University. She is a PhD candidate at the college of Mathematics and Physics, University of Science and Technology Beijing. Her research interests mainly focus on SIBs and hybrid supercapacitors.

Guozhen Shen received his BSc degree (1999) in chemistry from Anhui Normal University and PhD degree (2003) in chemistry from the University of Science and Technology of China. He joined the Institute of Semiconductors, Chinese Academy of Sciences as a professor in 2013. His current research focuses on flexible electronics and printable electronics, including transistors, photodetectors, sensors, and flexible energy storage and conversion devices.

Di Chen received her BSc degree (1999) in chemistry from Anhui Normal University and PhD degree (2005) in chemistry from the University of Science and Technology of China. She joined the University of Science and Technology Beijing as a professor in 2014. Her current research focuses on energy storage materials and devices.

Sb_2S_3/SnS_2/C异质结材料用于高性能钠离子电池

贾蕊[1,2], 李腊[2], 沈国震[2*], 陈娣[1*]

摘要 金属硫化物有着较高的理论容量，是钠离子电池极具潜力的负极材料. 然而, 这类材料在电化学反应过程中存在体积膨胀和反应动力学缓慢的缺点, 使得其循环和倍率性能较差. 本文通过在Sb_2S_3纳米棒上直接生长SnS_2纳米片并在其表面进一步包裹碳膜，制备了Sb_2S_3/SnS_2/C异质结构. 这种异质结构极大地提高了材料的稳定性, 并促进了离子和电子的运输. 研究结果表明，在六氟磷酸钠/二乙二醇二甲醚电解质体系中充放电循环600次后，Sb_2S_3/SnS_2/C复合电极材料在电流密度为1 A g^{-1}时表现出642 mA h g^{-1}的高可逆容量，并且在4 A g^{-1}时仍保留367.3 mA h g^{-1}的良好的倍率性能. 此外，为了研究该材料的电化学性能，本工作进一步探讨了钠离子在几种不同的电极材料和电解质中的扩散过程. 综上所述，Sb_2S_3/SnS_2/C异质结材料有望成为一种拥有广阔应用前景的钠离子电池负极材料.